Unique Spin Crossover Pathways Differentiated by Scan Rate in a New Dinuclear Fe(II) Triple Helicate: Mechanistic Deductions Enabled by Synchrotron Radiation Studies

*Matthew J. Wallis, Alexander R. Craze, Hikaru Zenno, Ryuya Tokunaga, Takahiro Taira, Hyunsung Min, Mohan M. Bhadbhade, Saroj Kumar Bhattacharyya, Ruoming Tian, Anne M. Rich, Shinya Hayami, Jack K. Clegg, Christopher E. Marjo, Leonard F. Lindoy and Feng Li**

Keywords: Spin crossover, dinuclear triple helicate, synchrotron, phase transition, scan rate

Abstract

The achievement of targeted properties in spin crossover (SCO) materials is complicated by often unpredictable cooperative interactions in the solid state. Herein, we report a dinuclear Fe(II) triple helicate **1**, which is a rare example of a SCO material possessing two distinct magnetic behaviors that depend upon the thermal scan rate. Desolvated **1** was seen to undergo spin transition (ST) which was complete following slow cooling (1 K min^{-1}), but incomplete ST (corresponding to 50% conversion) on fast cooling (10 K min^{-1}). The incomplete ST observed in the latter case was accompanied by a higher temperature onset of ST, differing from TIESST (Temperature-Induced Excited Spin-State Trapping) materials. The two SCO pathways have been shown to arise from the interconversion between two structural phases (**a** and **b**), with both phases having associated high spin (HS) and low spin (LS) states. SCXRD (Single Crystal X-ray Diffraction) experiments using controlled cooling rates and a synchrotron light source enabled short collection times (2-3 minutes per dataset) which has enabled the identification of a mechanism by which the slow-cooled material may fully relax. In contrast, fast-cooled materials exhibit disordered arrangements of multiple structural phases, which has in turn revealed that the [HS-LS] ↔ [LS-HS] equilibria are controllable in the solid by varying the scan rate. Such behavior has been previously observed in solution studies, but its control in solids has not been reported up to now. This study demonstrates how intermolecular cooperativity can allow multiple distinct magnetic behaviors, and provides some insight into how [HS-LS] ↔ [LS-HS] equilibria can be controlled in the solid state, which may assist in the design of next-generation logic and signaling devices.

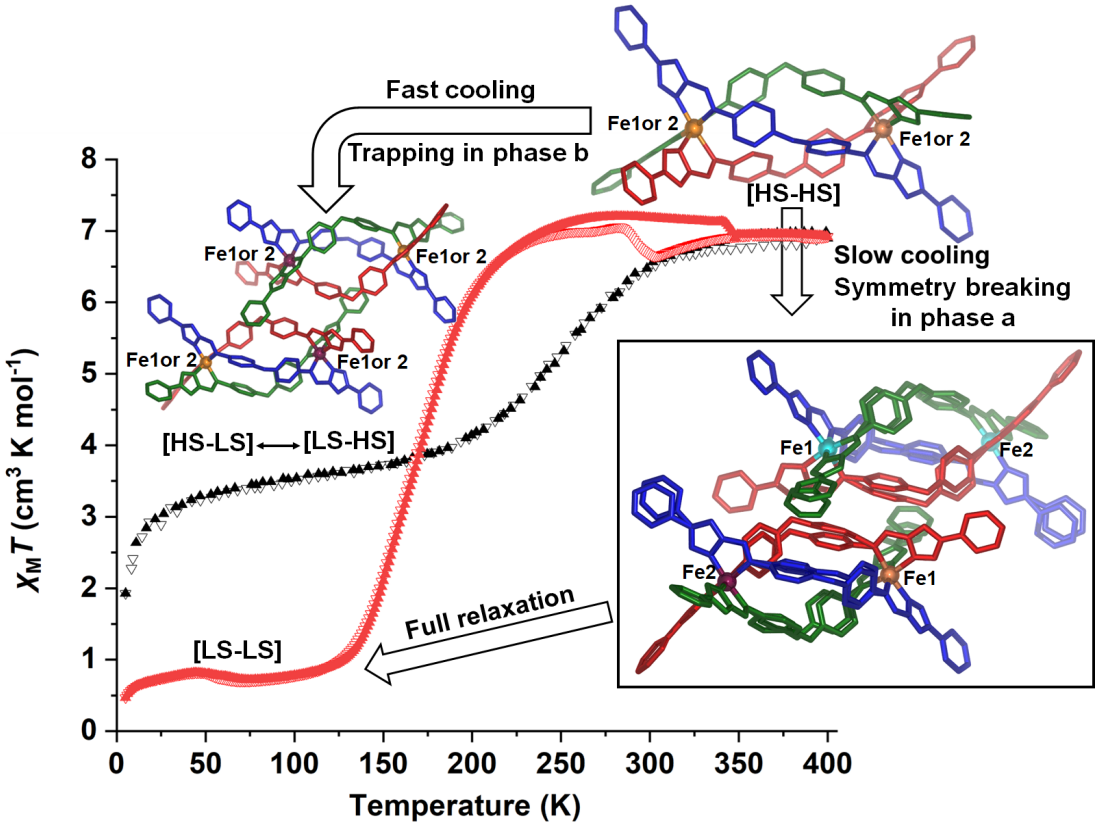

1. Introduction

Spin crossover (SCO) compounds are an exciting class of materials with a range of potential applications across diverse fields.[1-3] Such materials most commonly incorporate coordination complexes with $3d^{4\text{-}7}$ transition metal centers and intermediate ligand fields, and are thereby able to switch between high spin (HS) and low spin (LS) on application of external stimuli such as temperature, pressure and light irradiation.[1-12] SCO has been observed in both the solution and solid state, with the latter being markedly affected by the supramolecular environment present in the crystal lattice such as intermolecular contacts and steric factors, which consequently may give rise to cooperative behaviors that include both abrupt and hysteretic spin transitions (ST).[5] Of the possible metal centers available for use in SCO compounds, Fe(II) has been the most extensively employed. The easily distinguishable LS (S = 0) and HS (S = 2) states, as well as the manipulation

of these two states through variation of the coordination environment can result in large changes in the physical and magnetic properties. Most notably the change of bond lengths of approximately 10% from the LS to HS state typically occurs.[5-6]

The majority of the SCO studies so far have focused on the synthesis of mononuclear compounds, which simplifies the probing of intermolecular cooperativity.[9,12-13] Additionally, polymeric metal-organic frameworks (MOFs) have been well studied, wherein direct bonding connectivity may readily enhance cooperative effects in the solid.[14] On the other hand, discrete multinuclear SCO compounds offer a mixture of inter- and intramolecular cooperativity, which potentially provide multiple avenues for modulating the magnetic properties of SCO solids. Although mononuclear complexes have been widely used to probe intermolecular cooperativity,[9,12-13] multinuclear complexes displaying various topologies are also being extensively studied.[7] Within assemblies of multinuclear complexes the cooperative effects between metal centers occurring via their ligand backbone may tune their SCO properties, and ultimately result in switching behavior governed by a complex interplay between inter- and intramolecular cooperativity. Relative to polynuclear SCO complexes, dinuclear systems provide a simpler means for tuning these two sources of cooperative effects. The SCO profile of a given dinuclear complex can be associated with three different magnetic states: [HS-HS], [HS-LS]/[LS-HS] and [LS-LS]. The physical bridging of metal centers by ligand linkers means that in the intermediate [HS-LS]/[LS-HS] state, structural rearrangement at one metal center upon SCO influences the steric environment and ultimately the ligand field of the second metal ion. This may potentially stabilize, or destabilize the HS state, which can result in either abrupt SCO or gradual SCO for which there is little to no cooperativity, or in severe cases, trapping of the [HS-LS]/[LS-HS] at low temperature without the [LS-LS] state being formed. Such a structural rearrangement

with SCO has been associated with crystallographic symmetry breaking in several studies,[7,15-19] wherein structural rearrangement during SCO is severe enough to result in a change in the crystallographic phase of the material. The appearance of a phase change is, currently, fairly unpredictable. A change of phase can often accompany different packing patterns of structurally equivalent molecules or the formation of molecular isomers, and often lead to drastic effects on the SCO properties. With regards to dinuclear triple helicates, which take the form $[M_2L_3]$, the cooperativity is shared across their three separate ligand strands with identical structures. To date, most of the Fe(II) helicate structures exhibiting SCO properties involve an imidazolimine-based coordination environment.[20-29] Manipulation of the SCO properties in these dinuclear systems relies on the design of ligand structure(s) so as to induce a suitbale ligand field. Several distinct dinuclear triple helicates have been shown to exhibit spin switching, with different structures from those conjoining metal cations via ligand bridging.[14] Up to the present, the observation of two equivalent [HS-LS]/[LS-HS] species in equilibrium has been only reported for the solution state,[19] with no examples of [HS-LS] ↔ [LS-HS] equilibrium being reported for the solid state. Control of [HS-LS] ↔ [LS-HS] equilibria is desirable, as it may allow the generation of class II quantum cellular automata for signal and logic processes.[30,31]

Many spin-switching materials, particularly those possessing a highly cooperative SCO, have demonstrated magnetic profiles that depend on the scan rate at which magnetic susceptibility measurements are conducted. A thermal hysteresis can result from the magnetic susceptibility in responding to the altered temperature, with larger hysteresis often being produced at faster scan rates.[6] Another example of rate dependence on SCO is kinetic trapping of the HS state, where the high spin state is trapped by fast cooling.[32-34] For example Weber et. al. presented an Fe(II) SCO

compound that produced a loss of both the completeness of the ST and hysteresis with increased scan rate.[34]

In much rarer circumstances, altering the scan rate may also result in different structural pathways for the spin transition. For example, Real et. al.[35] presented a mononuclear structure that demonstrated two distinct hysteretic SCO profiles — differing in both $T_{1/2}$ values and hysteresis width — that were found to emerge at different scan rates. A polymeric example with similar behavior was reported by Zhang et. al.[36] Additionally, Yamasaki and Ishida[37] presented another mononuclear structure which was shown to have equivalent magnetic profiles on cooling, but heating at different scan rates allowed the differentiation of two distinct profiles. In these studies, differences in magnetic profiles were proposed to be the result of a phase transition, whereby two different LS phases shared the same HS phase. In this way the spin crossover profile was manipulated by a kinetically controlled structural phase change.

Herein, we report a rare example of a dinuclear SCO Fe(II) compound that possesses kinetic control of both the forward and reverse spin crossover pathways from [HS-HS] to [LS-LS]. The $[Fe_2\mathbf{L}_3](BF_4)_4$ helicate, herein denoted as **1**, was formed using ligand **L**, which features a bridging 4,4'-oxydianiline group, linking two 4-imidazoleimine coordination environments, each of which also bears a terminal pyridyl group. The complex may act as a metalloligand towards further metal ions, similar to our previous work.[38-43]

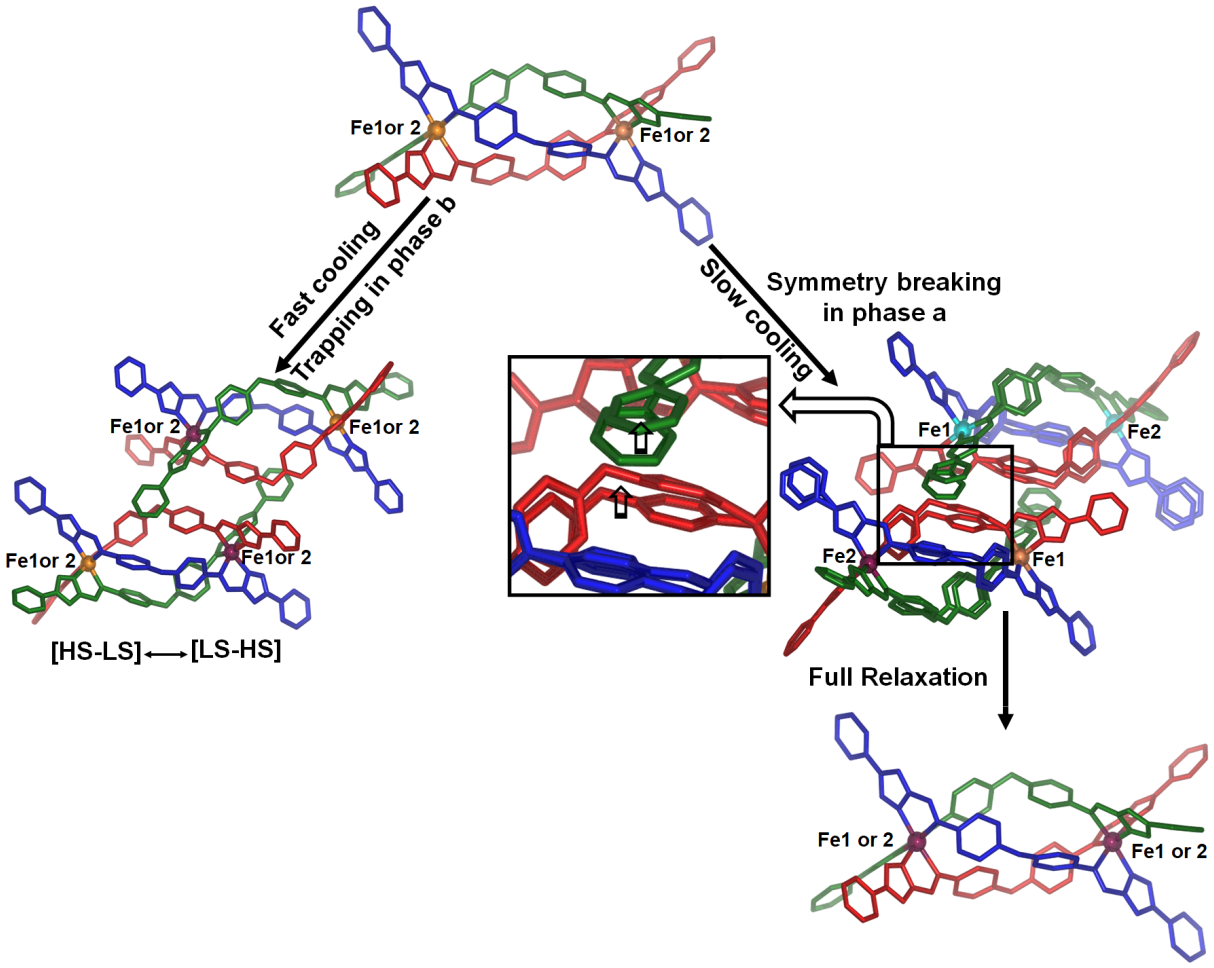

Figure 1. Schematic of the proposed mechanism for fast and slow cooling routes in **1**. Color code: Ligand **A** (red), ligand **B** (blue), ligand **C** (green), HS Fe (orange) MS Fe (cyan) and LS Fe (purple).

Two distinct SCO pathways were observed in single crystals with the former dependent on the scan rate of the temperature (Figure 1). Structural reorientation of key chemical moieties in the three semirigid linker ligands **L** upon SCO produces steric interactions, whereby adjacent helicate molecules in the lattice impose steric influences on one another. With sufficient time provided by slow cooling and a long collection period, ligand conformations allow a spin transition of one Fe(II) per helicate, forming the [HS-LS] state, whereas intermediate or flash cooling induces a spin

transition proceeding through a mixture of [HS-LS] and [LS-HS] helicates. At an intermediate scan rate of 4 K min^{-1}, an associated breaking of symmetry resulted in a combination of both of the above states being observed. In this way, the steric interactions imposed by structural reorientation may result in the observed kinetic differentiation of two structurally distinct SCO pathways which appear to allow the modulation of the lattice spin transitions. In thermal magnetic experiments of the desolvated sample, two distinct magnetic profiles were observed, coming about due to the conformation of the bulk solid to one of two phases, herein denoted **a** and **b**, each of which have distinct HS and LS states (Figure 2). That is, one magnetic profile is observed when the solid is in phase **a**, giving rise to **HS-a** ↔ **LS-a** spin transitions, while distinct behavior arises from the solid conforming to phase **b**, providing **HS-b** ↔ **LS-b** spin transitions. At the slow scan rate of 1 K min^{-1}, cooling enabled a phase transition from **HS-b** to **HS-a**, which underwent complete SCO to **LS-a**. At faster scan rates of 4, 7 and 10 K min^{-1}, little to no interconversion between the HS phases was able to occur, resulting in an incomplete ST from **HS-b** to **LS-b** with a higher T_{SCO}.

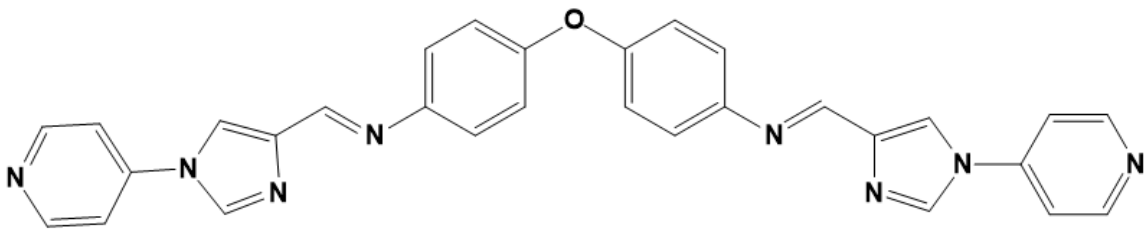

L

2. Results and discussion:

Synthesis and Characterisation

The reaction of 4,4-oxydianiline and 1-(pyridine-4-yl)-1H-imidazole-4-carbaldehyde in ethanol (EtOH) produced the desired ligand **L** in 79% yield. ^{1}H and ^{13}C NMR and high resolution electrospray ionization mass spectrometry (HR-ESI MS) confirmed the formation of the proposed **L** structure (Figure S1-S4). The HR-ESI mass spectrum demonstrated a major peak observed at *m/z* at 533.1523 $[L + Na]^{+}$ with the appropriate isotope pattern also observed (Figure S3).

The addition of iron(II) tetrafluoroborate to a suspension of **L** in acetonitrile (MeCN) followed by a slow vapor diffusion of diethyl ether into the reaction mixture produced orange plate crystals of **1** suitable for analysis. The HR-ESI mass spectrum demonstrated major peaks at *m/z* 410.5572 and 576.4459 which correspond to $[Fe_2L_3]^{4+}$ and $[Fe_2L_3(BF_4)]^{3+}$ respectively (Figure S5). The scanning electron microscopy - energy dispersive spectroscopy (SEM-EDS) spectrum confirmed the presence of C, N, F, O and Fe atoms. A mass change of -4.37% was calculated (Figure S7), consistent with the loss of 6 H_2O molecules per mole and in accordance with the CHN elemental analysis. SCXRD experiments confirmed the structure of **1** (Figure 1).

Magnetic Measurements

The magnetic susceptibility measurements including light-induced spin state trapping (LIESST) studies were undertaken on solvated and desolvated samples. Desolvated **1** showed interesting scan rate dependent behaviour (Figure 2), which is advantageous since desolvation is desirable in applied materials; it is easily maintained, as opposed to an optimal degree of solvation. In the 1 K min^{-1} cooling cycle, the onset of SCO occurred at 225 K, reaching $T_{1/2}$ at 169 K, and gradually reaching a local minimum of 0.70 cm^3 K mol^{-1} at 71 K. Low-temperature fluctuations were observed in the region below 80 K, with the cooling mode reaching an apex of 0.82 cm^3 K mol^{-1} at 47 K, and the heating mode locally apexing at 45 K with 0.81 cm^3 K mol^{-1}, relaxing to a local

minimum further along the heating mode. Additionally, the 1 K min^{-1} plots display a small reverse SCO event in the higher temperature range with a hysteresis loop of 54 K width (Figure 2b).

When the experiment is performed at faster scan rates, features associated with the primary SCO event and reverse SCO are drastically modified. In the cooling cycles of 4, 7 and 10 K min^{-1}, the reverse SCO is not observed, with the $\chi_M T$ declining consistently with that of the 1 K min^{-1} cooling scan, only until 303 K, where the slowest scan rate exhibited reverse ST (Figure 2b). The faster cooling scans continue to decrease in $\chi_M T$, reaching T_{SCO} at 252 K, which was retraced in each heating mode, and reaching approximately 50% conversion to the fully LS state, demonstrated by the gradually declining plateau region below 150 K. This may arise due to the occupation of the HS-LS state in all SCO molecules in the solid, or by conversion of half of the sample to LS-LS while the other half remains in HS-HS. In the 4 K min^{-1} cooling mode, there is a small rise in magnetic susceptibility, featuring a small hump at 50 K (3.60 cm^3 K mol^{-1}). The 4 K min^{-1} heating mode features a more distinguished hump, reaching a local maximum of 3.98 cm^3 K mol^{-1} at 56 K before again declining and retracing the corresponding cooling mode from 170 K (Figure 2c). In the region where reverse SCO is observed for the 1 K min^{-1} scans, the same feature is somewhat apparent, but obfuscated at 4 and 7 K min^{-1}, whereby $\chi_M T$ rises away from the corresponding cooling mode plots above 270 K, reaching a peak of 7.02 cm^3 K mol^{-1} at 325 K in the 4 K min^{-1} heating mode and 6.97 cm^3 K mol^{-1} at 322 K with 7 K min^{-1} heating. In the region above 350 K, there is little differentiation between any of the scan rates.

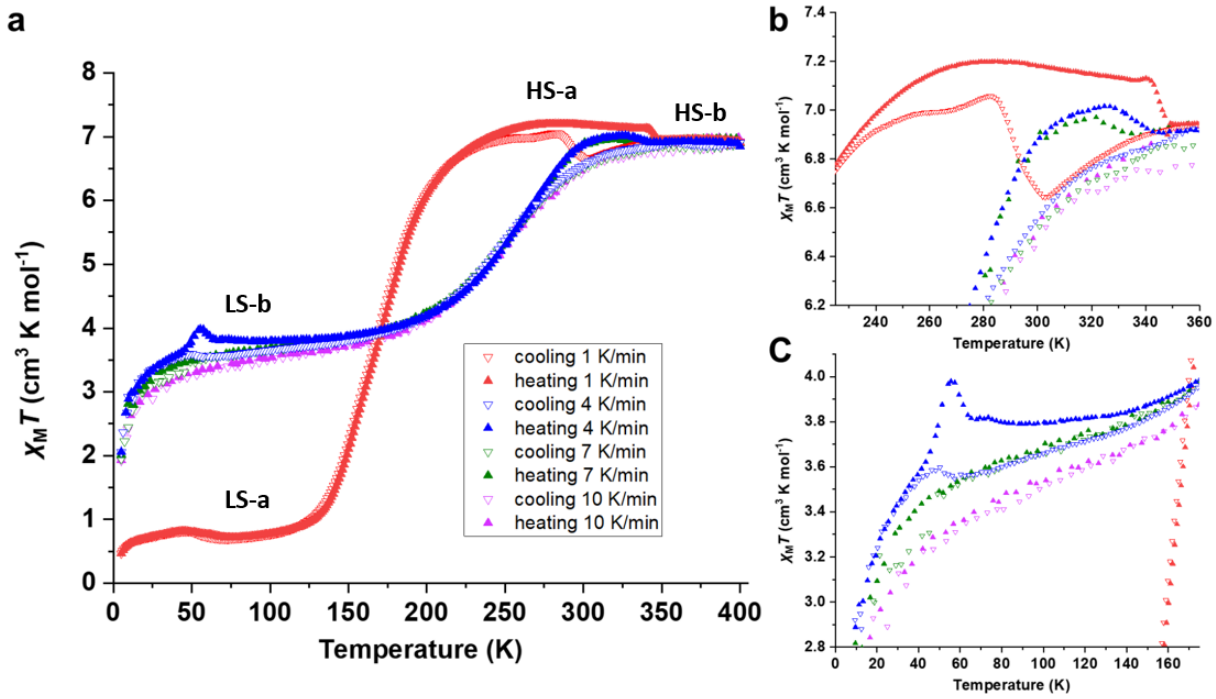

Figure 2. a) Magnetic susceptibility curves for desolvated **1** at sweep rates of 1, 4, 7 and 10 K min^{-1}. b) Close-up of magnetic susceptibility above 230 K. c) Close-up of low-temperature magnetic susceptibility for scan rates of 4, 7 and 10 K min^{-1}.

The magnetic profiles of all scan rates align well only for the temperature region higher than the reverse SCO event. In the cooling modes, all spin transition curves track well with each other until the reverse ST event seen to begin at 302 K for the 1 K min^{-1}. This reverse ST event is indicative of a phase change between two distinct [HS-HS] phases, which we denote **HS-a** and **HS-b**. In the slowest scan rate of 1 K min^{-1}, the sample is able to fully convert from **HS-b** to **HS-a**, before the bulk of the sample converts from **HS-a** to the [LS-LS] **(LS-a)** configuration by the primary ST event. In the fastest cooling rate of 10 K min^{-1}, no interconversion between **HS-b** to **HS-a** is able to take place, and the solid then converts via a different spin transition pathway from **HS-b** to the [HS-LS] state **(LS-b)**. Furthermore, in the 4 and 7 K min^{-1} scans, the deviation between the heating

and cooling modes upper region of the primary ST event may be due to a conversion from **HS-b** to **HS-a** in the temperature region in which this phase is stable, before the increase in temperature destabilized the **HS-a** phase and the bulk of the solid returns to the **HS-b** phase.

In addition, Mössbauer measurements revealed that both **1**·6H_2O and desolvated **1** are fully LS at 78 K, and fully HS at 298 K (S2.1). The magnetic susceptibility measurements for the solvated sample showed that **1**·6H_2O undergoes complete spin transition at scan rates 1 and 4 K min^{-1} (S2.2). Further, LIESST studies demonstrated that **1** undergoes a photomagnetic response with exposure to red (800 nm) and green (532 nm) light (S2.3). Raman studies performed on **1**·6H_2O with a green laser (514 nm) and controlled cooling of 1 K min^{-1} revealed marker peaks of the HS and LS states, and increased laser power at 100 K resulted in spectral data consistent with the HS state (S3).

Magneto-structural correlations - Kinetic control of the SCO mechanism:

To unambiguously label the crystal structures herein, nomenclature is introduced which specifies the temperature and scan rate of each collection in the form [compound]@temperature/[scan rate], where the scan rates are referred to as relax, 1 K min^{-1}, 2 K min^{-1}, 4 K min^{-1} and flash. For example, the structure of **1** collected at 150 K after cooling at 4 K min^{-1} will be labeled **1**@150/4. **1** crystallized in the triclinic space group *P-1* with four BF_4^- counterions, four MeCN, one diethyl ether (Et_2O) molecule and 5.75 H_2O per helicate. A solvent mask was applied in all structures except **1**@100/relax, which had no solvent accessible voids. The $[Fe_2\mathbf{L}_3]^{4+}$ helicate architecture consists of three ditopic imidazoleimine ligands coordinating to two Fe(II) centers, one at each end of the resulting complex. The coordination environment of each Fe(II) center is composed of three imidazoleimine donor groups, with six nitrogens coordinating overall so that the three imine and

three imidazole donors each adopt facial orientation to give a distorted octahedral arrangement. Distal non-coordinating pyridyl groups provide H-bonding capacity towards the periphery of the structure. These groups, along with the benzene moieties, engender key intermolecular interactions between helicate molecules that dictate the interhelical spacing and steric interactions in the resulting lattice. The packing and resulting steric interactions in helical SCO molecules have been shown previously to have a marked effect on the nature of the ST.[22,27] The three ligands used to form the helicate structure (**A**, **B** and **C**) were found to each be involved in a different set of intermolecular interactions (Figure 3). Ligand **A** forms a continuous 1D chain, stabilized by N···HC hydrogen bonds between pyridyl N atoms and imidazole CH groups, as well as π-π interactions between terminal pyridyl groups of adjacent helicates. The terminal segment of ligand **B**, proximal to Fe1, also participates in a substantially offset π-π interaction with an equivalent terminal group of a neighboring helicate. On the other hand, the distal segment of ligand **B** near the Fe2 center does not participate in any π-π stacking, with the neighboring ring systems being heavily offset reflecting the adjacent positions of BF_4^- counter ions. With respect to ligand **C**, the pyridyl group at the Fe1 end of the helicate lies close to the central O atom of ligand **A** on an adjacent helicate of opposite helicity (Table S3), while the pyridyl group at the Fe2 end makes no close intermolecular contacts to adjacent helicates. For single crystals of **1**, SCO may occur at either Fe center in the helicate (see below), but complete transition to the LS-LS state is inhibited at 100 K, unlike the situation occurring for **1**·$6H_2O$ (S2.2) and desolvated **1** (Figure 2). The inhibition may be influenced by the position of the Et_2O molecule, which lies between the terminal pyridyl of ligand **A** at the Fe1 end and the terminal pyridyl of ligand **B** at the Fe2 end.

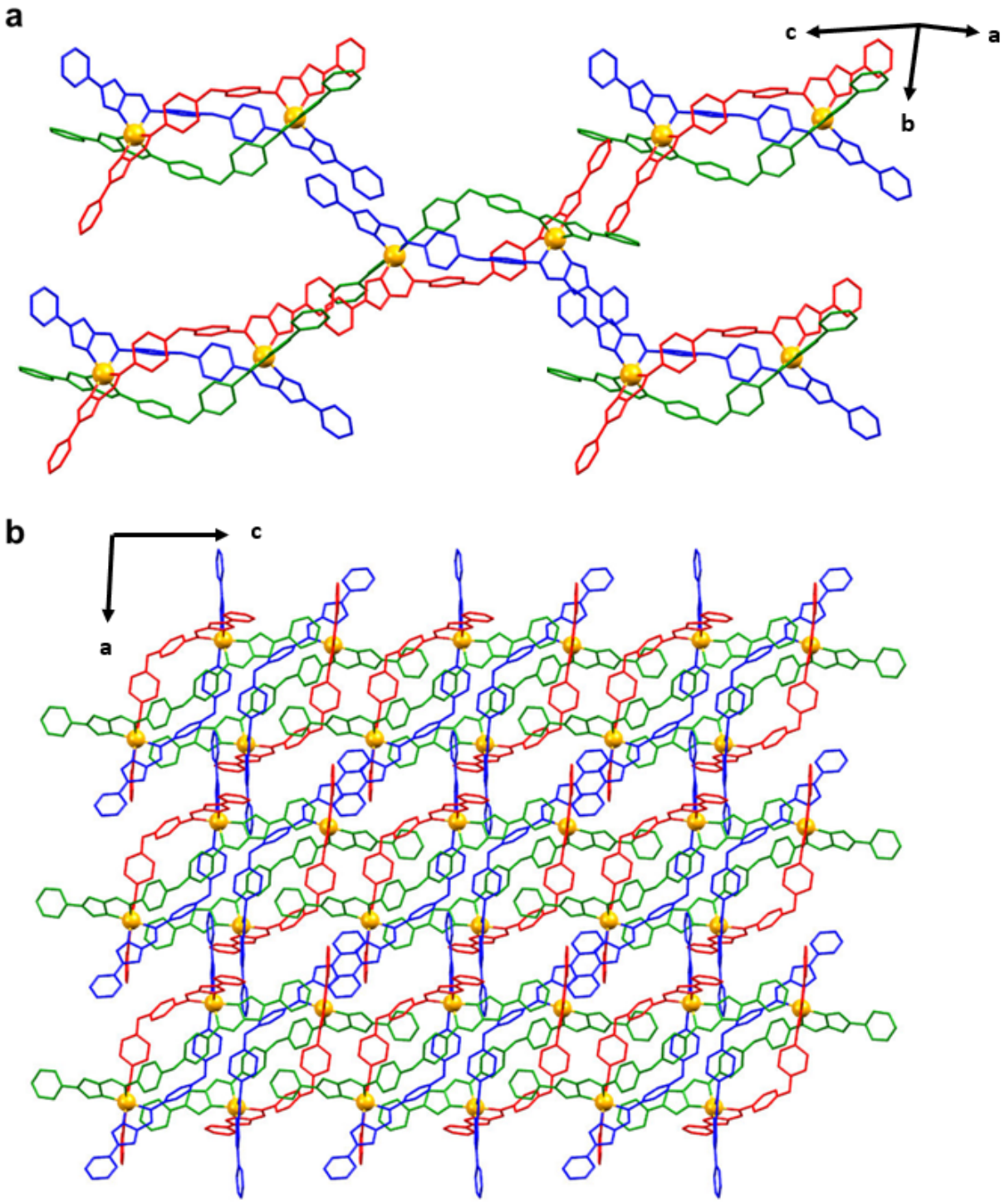

Figure 3. a) Crystal packing image of **1**@250 shown along the cell direction vector (1, 0, 1). b) Crystal packing of **1**@250 shown in the *b*-axis direction. HS Fe centers are orange, ligand **A** red, ligand **B** blue, ligand **C** green.

Two distinct structural pathways were observed for the relaxed and the flash scan rates when cooled to 100 K, while **1**@100/4 showed a structure having undergone both pathways in equal part. At 250 K the average coordinate bond length (*D*) of 2.20 and 2.19 Å were found for Fe1 and Fe2, respectively; indicative of the HS state at both metal centers. The respective Σ values[5] of 88.7 and 85.1° for Fe1 and Fe2 are also consistent with the assignment of the HS state. First, when cooled to 100 K allowing for relaxation (**1**@100/relax), the *D* and Σ values measured for Fe1 were 2.19 Å and 82.6°, while those for Fe2 were 2.00 Å and 58.4°. This is indicative of a HS-LS state at 100 K when cooled in this manner. Analysis of the helicate packing shows tighter packing of adjacent 1D chains along the crystallographic *b*-axis (Figure 4), concomitant with higher packing density. This is demonstrated by the markedly shorter *b*-axis and cell volume, which are 18.18 Å and 5744 Å^3 in the 250 K structure, respectively, and drop to 16.73 Å and 5358 Å^3 in **1**@100/relax (Table 1). Furthermore, the **1**@100/relax packing coefficient of 47.28% — compared to 44.15%, 46.28% and 46.06% for **1**@250, **1**@100/4 and **1**@100/flash respectively — indicates a more tightly packed arrangement (S4). The Fe2 centers that undergo a spin transition in **1**@100/relax are connected along the 1D chains described above by terminal π-π and N···HC contacts for ligand **A**, as well as close packing of the pyridyl groups of ligand **B** at the Fe2 end of the helicate, as shown in Figure 4.

Table 1. Selected parameters of *b*-axis, *V*, average Fe-N distance (*D*), Σ and crystal packing coefficient of **1**.

Structure (**1**@...)	***b*** **(Å)**	**Volume (Å^3)**	**Packing (%)**	***D*** **(Å)**	**Σ (°)**
100/relax	16.73	5358	47.28	**Fe1**: 2.19, **Fe2**: 2.00	**Fe1**: 82.6, **Fe2**: 58.4

100/flash	17.72	5495	46.06	**Fe1**: 2.15, **Fe2**: 2.07	**Fe1**: 78.2, **Fe2:** 70.6
250	18.18	5744	44.15	**Fe1**: 2.20, **Fe2**: 2.19	**Fe1**: 88.7, **Fe2**: 85.1
100/1	17.82	5533	45.74	**Fe1**: 2.13, **Fe2**: 2.08	**Fe1**: 80.0, **Fe2**: 73.2
150/1	17.91	5586	45.28	**Fe1**: 2.16, **Fe2**: 2.11	**Fe1**: 84.4, **Fe2**: 74.6
200/1	18.08	5678	44.80	**Fe1**: 2.19, **Fe2**: 2.19	**Fe1**: 87.4, **Fe2**: 84.3
100/2	17.72	5527	45.77	**Fe1**: 2.14, **Fe2**: 2.08	**Fe1**: 76.8, **Fe2**: 70.5
150/2	17.83	5583	45.36	**Fe1**: 2.15, **Fe2**: 2.08	**Fe1**: 78.6, **Fe2**: 70.5
200/2	18.07	5676	44.07	**Fe1**: 2.19, **Fe2**: 2.19	**Fe1**: 89.1, **Fe2**: 85.7
100/4	17.69	5478	46.28	**Fe1**: 2.18, **Fe2**: 2.00, **Fe1':** 2.14, **Fe2':** 2.15	**Fe1**: 79.4, **Fe2**: 61.1, **Fe1':** 76.8, **Fe2':** 83.1
150/4	17.77	5524	45.87	**Fe1**: 2.18, **Fe2**: 2.02, **Fe1'**: 2.17 **Fe2':** 2.17	**Fe1**: 79.6, **Fe2**: 62.8, **Fe1':** 83.2, **Fe2':** 84.9
200/4	17.98	5643	45.06	**Fe1**: 2.19, **Fe2**: 2.18	**Fe1**: 86.9, **Fe2**: 83.3

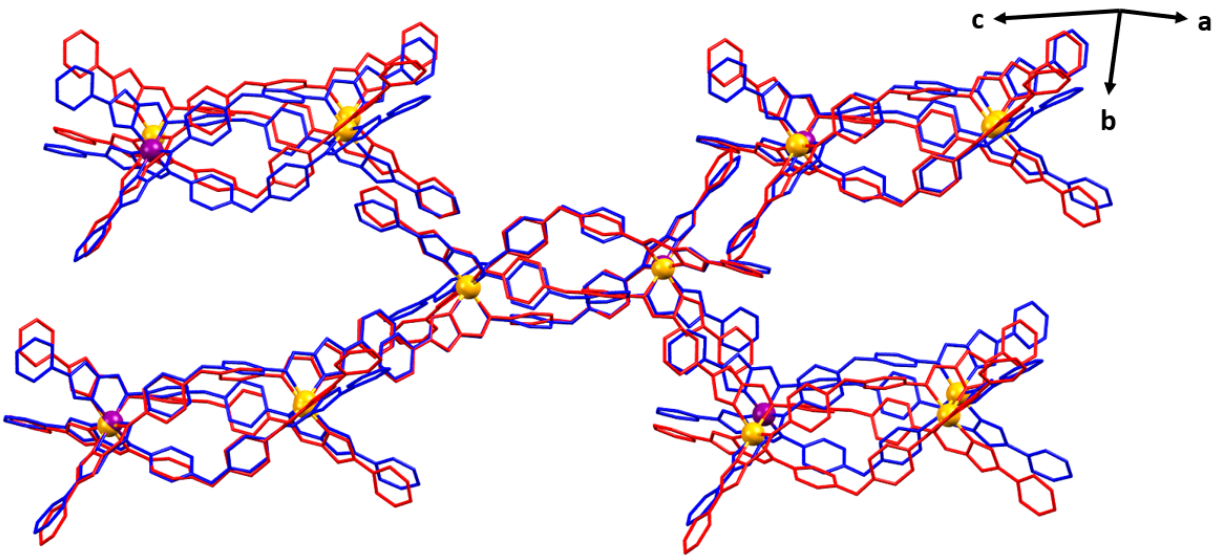

Figure 4. Crystal Structures of **1**@100/relax (blue), with HS Fe1 (orange) and LS Fe2 (purple) overlaid with **1**@250 (red) with both Fe centers in HS state (orange). Molecules pack closer together along the *b*-axis in **1**@100/relax than **1**@250.

On the other hand, when the sample was flash cooled to 100 K (**1**@100/flash), the observed values of *D* and Σ were 2.15 Å and 78.2° for Fe1, and 2.07 Å and 70.6° for Fe2. This may be interpreted as a superposition of HS and LS Fe centers at both crystallographically distinct Fe centers, and will be referred to as the MS-MS state from here on (where MS refers to a mixed population of HS and LS states). This suggests that, in contrast to the **1**@100/relax structure above, flash cooling promotes the transition of the Fe1 or Fe2 centers of different helicates, with around half of the helicates having undergone a transition to the HS-LS, and a small population transitioning to the LS-HS state at 100 K, rather than solely selective transition of Fe2 throughout the material. Interestingly, the *b*-axis (17.72 Å) and cell volume (5495 $Å^3$) are larger than that of **1**@100/relax which, along with a packing coefficient of 46.06%, suggests more space is present between adjacent helicates (Figure 5).

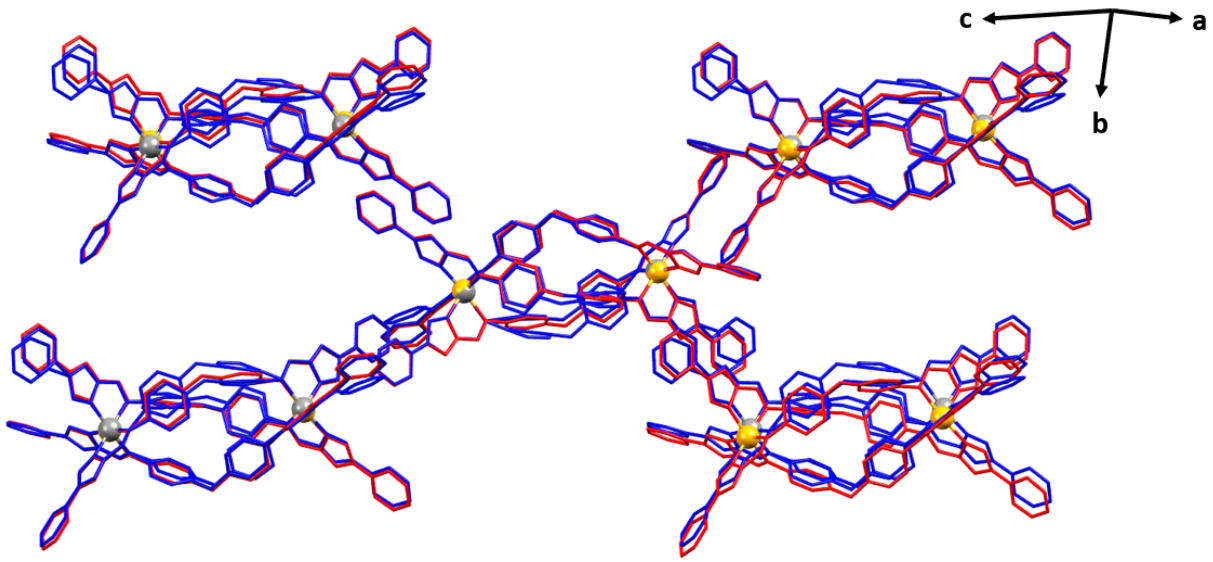

Figure 5. Overlay of **1**@100/flash (blue) with MS Fe centers (gray), and **1**@250 (red) with HS Fe centers (orange). Contraction along the *b*-axis in **1**@100/flash is minor relative to that of the **1**@100/relax structure.

Finally, cooling at 4 K min^{-1} caused symmetry breaking in the lattice, whereby *P-1* symmetry persisted with a doubled *c* axis, observed between 150 and 100 K, leading to an additional helicate being resolved per asymmetric unit. The same analysis of each distinct helicate in **1**@100/4 showed that one helicate adopted the HS-LS state (Fe1, D = 2.18 Å, Σ = 79.4°; Fe2, D = 2.00 Å, Σ = 61.1°) similar to **1**@100/relax, while the additional symmetrically inequivalent helicate was found to be MS-MS (Fe1', D = 2.14 Å, Σ = 76.8°; Fe2', D = 2.15 Å, Σ = 83.1°) similar to the situation in **1**@100/flash. That is, the **1**@100/4 showed a pathway combining that of the relaxed and flash cooled samples, where both pathways to SCO are observed simultaneously. The HS-LS helicates pack in 2D sheets parallel to the *ab* plane, interspaced with parallel 2D sheets of MS-MS helicates (Figure 6).

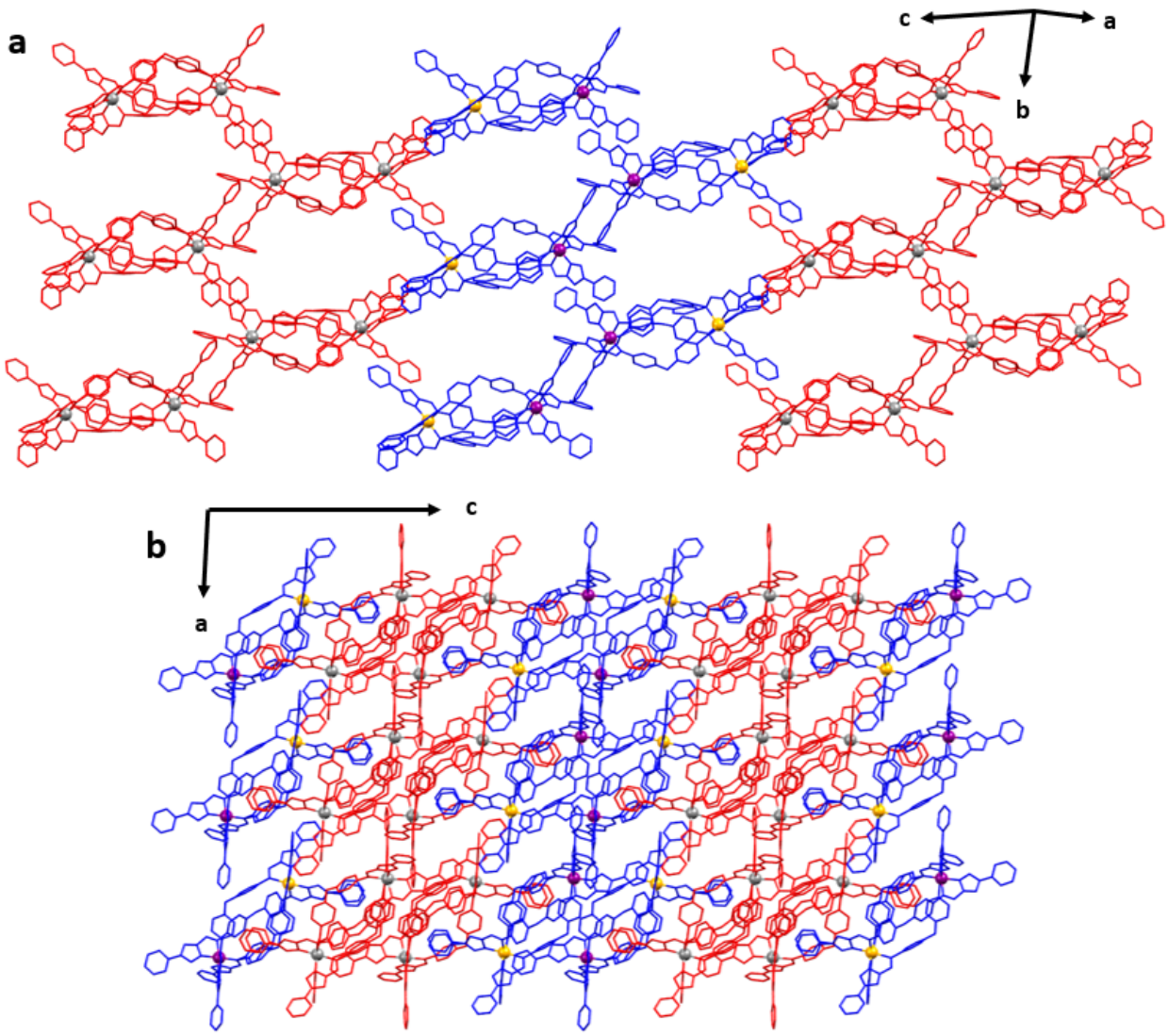

Figure 6. a) Crystal packing image of **1**@100/4 shown along the cell direction vector (2, 0, 1). b) Crystal packing of **1**@100/4 shown in the *b*-axis direction. Helicates (HS-LS) are shown with blue ligands, HS Fe1 and LS Fe2 centers in these helicates are orange and purple, respectively. Helicates trapped in MS-MS are shown in red with gray Fe centers.

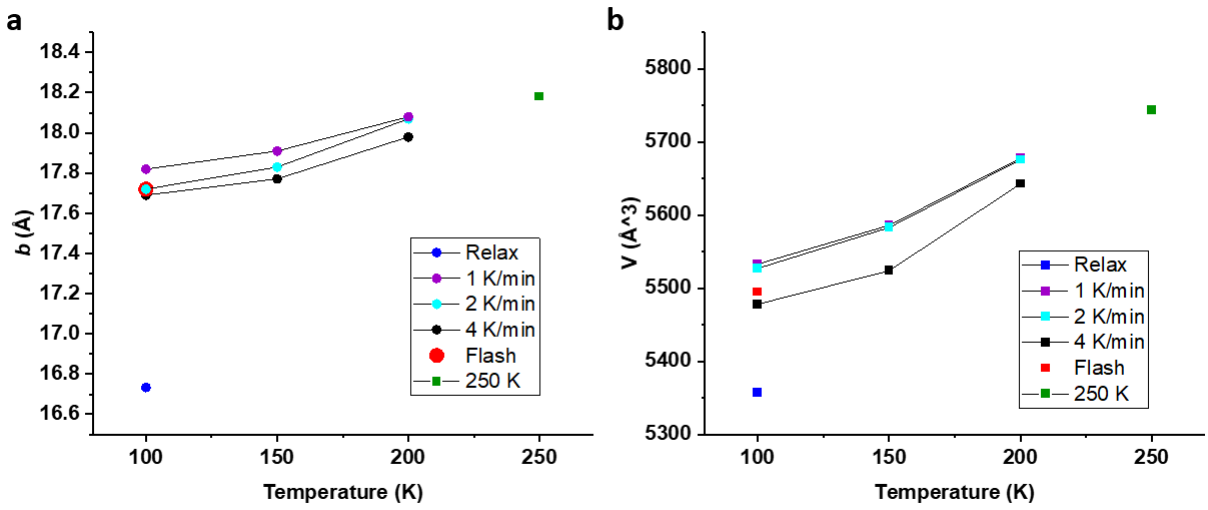

Figure 7. a) *b*-axis length with respect to temperature for different cooling rates. b) *V* with respect to temperature for a variety of cooling rates.

The supramolecular arrangement of the helicates for different cooling rates provides an interesting comparison. In this regard, the packing of adjacent 1D chains of **1**@100/relax is distinct from the other scan rates, with a markedly shorter *b*-axis and cell volume, which are 18.18 Å and 5744 Å^3, respectively in **1**@250, but drop to 16.73 Å and 5358 Å^3 in **1**@100/relax (Figure 7). On the other hand, the flash cooled material (**1**@100/flash) gave values for *b* and *V* of 17.72 Å and 5495 Å^3, and the 100 K structures at cooling rates of 1, 2 and 4 K min^{-1} showed similarly expanded lattices (compared to **1**@100/relax). As described above, the *b*-axis direction corresponds to important intermolecular interactions involving ligands **A** and **B** which are related to the spacing of 1D chains in the lattice, with dense packing observed for **1**@100/relax and less dense packing being observed for rapid and flash cooled structures (Figures 4 and 5). These results suggest that there may be some slow rearrangement of the structure that prohibits 1D chains from approaching each other at faster scan rates.

The helical packing, intermolecular interactions and changes in ligand conformation were compared for the above three pathways as a function of temperature. This was undertaken in an attempt to pinpoint any structural features that may be responsible for promoting the different pathways for SCO at different scan rates. First, in order to quantify the steric effects which may participate in the spin transition dynamics, the molecular volume of the helicates and the crystal packing coefficients (the percentage value of crystal volume occupied by the helical structures) were calculated (Figure 8). At 250 K, a packing coefficient of 44.15% was determined, while **1**@100/relax was found to have a value of 47.28% and **1**@100/4 and **1**@100/flash presented values of 46.28% and 46.06% respectively. This represents a significant difference between the HS-LS structure obtained after slow relaxation and both the intermediate and flash cooled structures. The molecular volume of the helicate measured at 250 K before cooling was 1267.6 $Å^3$, which reduced rather insignificantly — to 1265.3 $Å^3$ in **1**@100/relax for example. This suggests that the higher crystal packing coefficient of the HS-LS structure is related to tighter packing of the helicate molecules in the lattice, as opposed to changes in the molecular volume of individual helicates.

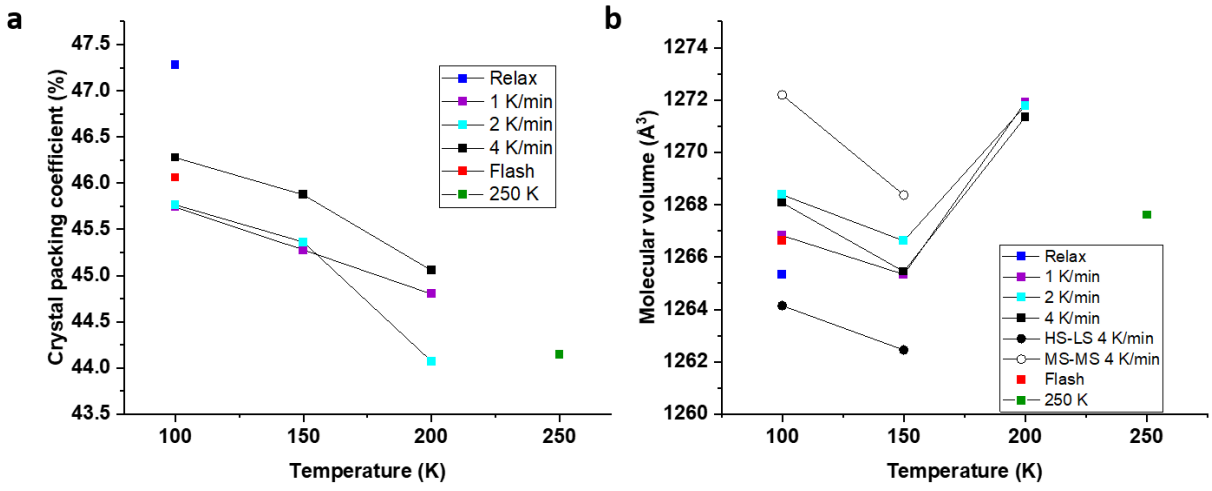

Figure 8. a) Crystal packing coefficient versus temperature. b) Molecular volume of **1** in each crystal structure.

Reorientations of the coordination environment upon spin transition in either Fe center of the helicate induce different reconfigurations within each ligand. These reorientations impose varying degrees of both intramolecular strain within the helicate and steric strain on adjacent helicates, which, in turn, may allow or inhibit the different pathways of spin transition. The steric effects influencing the crystal lattice may be related to the dynamics of molecular reorientation of individual helicate molecules. Reconformations of ligand molecules in neighboring helices are often seen to have a drastic effect on the cooperative or anticooperative effects observed in a transitioning solid.[44] As such, several parameters were calculated from the crystal structural data to describe the behavior of each ligand throughout the respective variable temperature (VT) experiments. As the coordinating sections of the ligand are less able to reorient, the terminal pyridyl and internal benzene groups are the moieties that are most likely to provide the greatest reorientation to relieve the intramolecular strain required for the structure to undergo SCO.

The helicate can be divided into components, with the orientation of each component used to provide insight into the overall conformation achieved by different parts of each ligand. The linker moieties were modeled using linker torsion (S5.1), which indicates the degree of twist of each of the benzene rings, relative to a reference plane describing the linker segment overall. The angle between the intermetallic axis and the axis defined by the two coordinating N atoms in each chelate ring was taken, and this was further deconstructed into pitch and yaw angles to more specifically indicate the direction of the reorientations in the chelate groups (S5.2-S5.3). By a similar methodology, angles between the intermetallic axis and the secondary bond axes were calculated. Here, the secondary bond axis refers to the interval between N atoms in terminal pyridines, and

the C atoms opposite in the ring (N1 - C3 or N8 - C28), which reflects the direction in which a coordinate bond from the secondary donor sites may form with respect to the intermetallic axis, similar to methods employed in our previous work (S5.2).[43] This allows for quantification of the degree of spreading of the terminal pyridyl groups. Since the coordinating imidazoleimine and the terminal pyridine are both rigid groups, the spread of the secondary bond axes is closely linked to the orientation of the internal chelating section of the ligand. All of these parameters are defined such that they refer to an internal structural feature for consistent comparison; either the intermetallic axis, or in the case of linker ring torsions, a reference plane describing the linker orientation.

Following analysis of the structural measurements (Table 2) we are able to suggest a mechanism by which slow cooling allows the lattice of **1** to undergo a transition to [HS-LS] in the full population of helicate molecules in the solid, while faster cooling inhibits this transformation. Several ligand reconformations are demonstrated in the **1**@100/relax structure, which differ significantly from the 250 K structure (Table 2). One key feature is that the linker segment of ligand **A** repositions with a transition of Fe2 to LS. This occurs due to the rearrangement of the chelate group of **A** at Fe2, which changes the pitch to negative, and causes the benzene rings in **A** to exchange torsion values (Table 2). This, along with motion towards the terminal **C** pyridyl at Fe1 of an adjacent helicate, may induce a transition of the adjacent Fe1 to LS, due to the semi-rigid connection between the terminal pyridine and chelating imidazoleimine. This is demonstrated in the kinetically trapped **1**@100/4 structure through the low Fe1 octahedral distortion parameters. Additionally, the rearrangement of the **C** imidazole group skews the orientation of the CH group associated with the terminal N···HC hydrogen bond, weakening the contact between Fe1 centers along the 1D chains, which may contribute to the loss of inversion symmetry across these sites

(S6). Further reorientation in ligand groups puts into effect an overall supramolecular rearrangement. Transitioning the bulk of helicates in the solid to the [HS-LS] state instigates a significant decrease in **B** yaw at both ends of the helicate which allows terminal pyridyl groups of **B** to draw inwards and lower the secondary bond axis values of **B**. This in turn leads to the compression of 1D chains towards each other along the *b*-axis, as shown above.

Table 2. Selected geometric parameters describing the orientations of helicate components (See S5). 1 K min^{-1} values are shown to compare with those obtained at the extreme ends of the temperature range.

Structure (**1**@...)	***A** torsion[a] (°)	**A** Pitch[b] (°)	**A** Yaw[c] (°)	**B** Yaw[c] (°)	***A** Secondary bond axis[d] (°)	***B** Secondary bond axis[d] (°)
100/relax	**Fe1:** 61.7, **Fe2:** 32.8	**Fe1:** 6.9, **Fe2:** -2.8	**Fe1:** 33.4, **Fe2:** 33.0	**Fe1:** 34.0, **Fe2:** 38.0	**Fe1:** 44.0, **Fe2:** 44.2	**Fe1**: 32.4, **Fe2:** 46.1
100/flash	**Fe1:** 45.8, **Fe2:** 50.5	**Fe1:** 3.2, **Fe2:** 1.6	**Fe1:** 32.5, **Fe2:** 34.5	**Fe1:** 33.2, **Fe2:** 35.7	**Fe1:** 42.6, **Fe2:** 51.8	**Fe1:** 42.4, **Fe2:** 48.4
100/1	**Fe1:** 40.4, **Fe2:** 57.0	**Fe1:** 1.9, **Fe2:** 1.3	**Fe1:** 33.1, **Fe2:** 35.1	**Fe1:** 33.4, **Fe2:** 34.8	**Fe1:** 42.7, **Fe2:** 51.5	**Fe1:** 43.3, **Fe2:** 47.4
150/1	**Fe1:** 35.7, **Fe2:** 59.6	**Fe1:** 2.2, **Fe2:** 1.3	**Fe1:** 32.3, **Fe2:** 35.2	**Fe1:** 33.1, **Fe2:** 35.2	**Fe1:** 42.7, **Fe2:** 52.0	**Fe1:** 43.1, **Fe2:** 48.4
200/1	**Fe1:** 31.5, **Fe2:** 60.0	**Fe1:** 2.2, **Fe2:** 2.6	**Fe1:** 31.6, **Fe2:** 35.4	**Fe1:** 33.3, **Fe2:** 34.1	**Fe1:** 43.2, **Fe2:** 53.8	**Fe1:** 43.5, **Fe2:** 52.7
250	**Fe1:** 31.1, **Fe2:** 60.0	**Fe1:** 2.3, **Fe2:** 2.5	**Fe1:** 31.7, **Fe2:** 35.6	**Fe1:** 33.4, **Fe2:** 34.0	**Fe1:** 43.5, **Fe2:** 54.2	**Fe1:** 43.5, **Fe2:** 52.4

[a] The linker torsion angle measured from planes of each benzene group linked to a reference plane, identifying the degree of twist the linker region adopts at each end of the helicate.

[b] Pitch specifies the back and forth rocking orientation of the chelate groups in relation to the intermetallic axis.

[c] Yaw specifies the side-to-side twisting orientation of the chelate rings relative to the intermetallic axis.

[d] The secondary bonding axis measures the orientation of the terminal pyridine groups with respect to the intermetallic axis.

* In structures exhibiting orientational disorder, the parameter values were calculated for each part, and those values were scaled by the occupancy of the respective part and summed to provide the stated value.

The trends in unit cell shrinkage and contraction along the *b*-axis were confirmed in **1**·6H_2O and desolvated **1** using VT-PXRD with controlled ramping rates of 1 and 4 K min^{-1} (Figure 9a and b). In **1**·6H_2O, the higher values of *b* and *V* are consistent with the population of the lattice in the fully HS state. Cooling modes of both 1 and 4 K min^{-1} showed a marked decrease in *b* and *V* upon cooling to 150 K, with *b* reaching 16.4 Å at both scan rates, and *V* reaching 5186 $Å^3$ and 5224 $Å^3$ with 1 and 4 K min^{-1} cooling, respectively. As cooling cycles progress down to 40 K, the cell continues to shrink, with *b* and *V* respectively reaching minimum values of 16.3 Å and 5056 $Å^3$ with 1 K min^{-1} cooling, with similar values of 16.3 Å and 5043 $Å^3$ observed with 4 K min^{-1} cooling. In the heating mode of 1 K min^{-1}, the *b*-axis length tracked with that observed in the cooling mode, with some deviations while more significant deviations were observed in the *V* plot. Heating at 4 K min^{-1} provided an interesting result at 60 K, where the cell was seen to expand, with *b* and *V* measured at 16.6 Å and 5342 $Å^3$, respectively. This is consistent with the magnetic susceptibility curve of **1**·6H_2O measured at 4 K min^{-1}, which displayed a peak in $\chi_M T$ of 1.04 cm^3 K mol^{-1} at 59 K (Figure S9). The nature of these low-temperature dynamics is difficult to qualify, but they may arise due to interconversion between **LS-a** and **LS-b** phases at low temperatures, facilitated by an intermediate spin transition, which is also suggested by magnetic susceptibility measurements (S2.2). As the heating cycle continued at 4 K min^{-1}, *b* and *V* continued to grow, reaching HS values at 200 K and above.

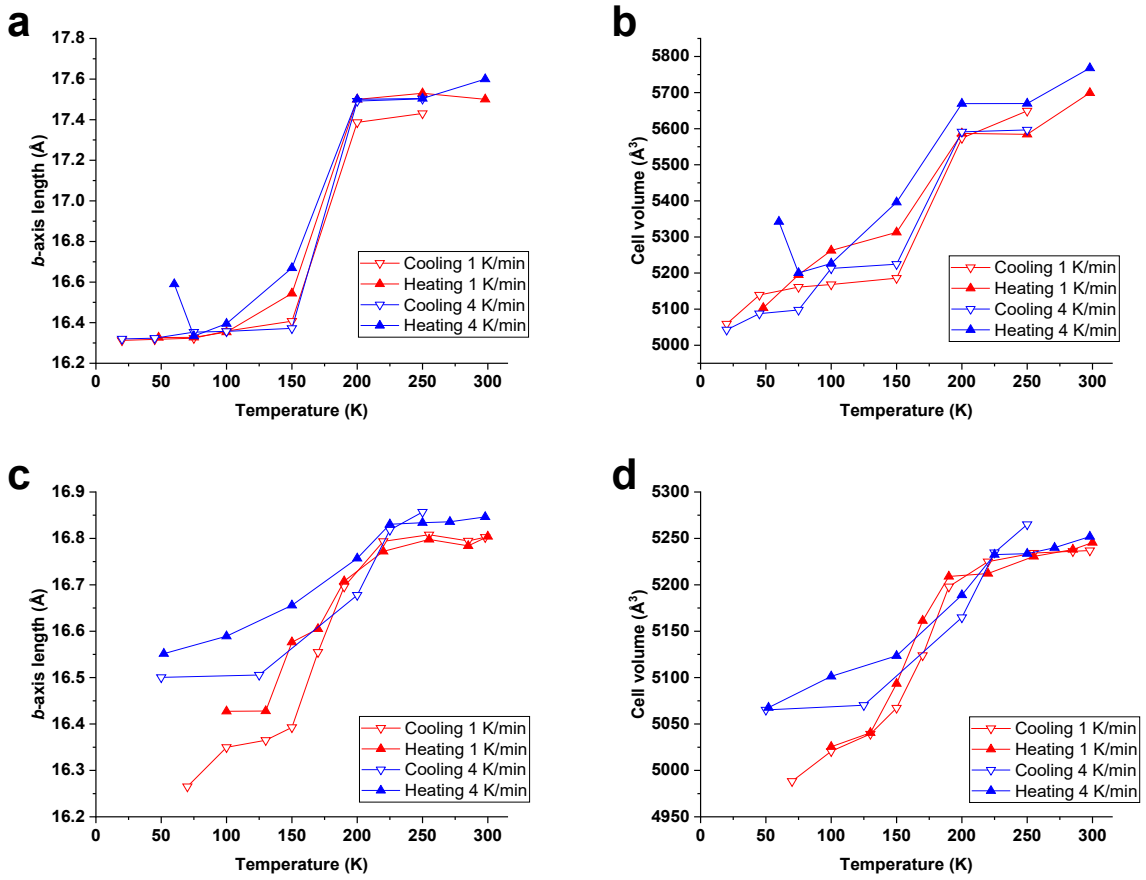

Figure 9. Selected lattice parameters versus temperature for **1**·6H_2O and desolvated **1** from VT-PXRD experiments in the heating and cooling modes at the scan rates 1 and 4 K min^{-1}. Sweeps were performed in the order: 1 K min^{-1} cooling (▽), 1 K min^{-1} heating (▲), 4 K min^{-1} cooling (▽), 4 K min^{-1} heating (▲). a) Plot of **1**·6H_2O *b*-axis length. b) Plot of **1**·6H_2O cell volume *V*. c) Plot of desolvated **1** *b*-axis length. d) Plot of desolvated **1** cell volume *V*.

More distinct variation between the two chosen scan rates was observed in the PXRD experiments of desolvated **1** (Figure 9c and d). In the 1 K min^{-1} cooling cycle, the 298 K structure provided *b* and *V* values of 16.8 Å and 5237 $Å^3$, respectively, indicative of the bulk desolvated sample being fully HS. These values remained fairly constant, until they began to drop sharply at 190 K and below. The cell continued to shrink to a minimum *b*-axis length of 16.3 Å and a volume

of 4988 Å^3 at 70 K, indicating that all or most of the sample was in the [LS-LS] state. The heating mode of 1 K min^{-1} varied slightly from the cooling mode, but overall reproduced the same general plot shape, reaching *b* and *V* values of 16.8 Å and 5246 Å^3 at 300 K. The 4 K min^{-1} cooling mode, which was performed immediately after the 1 K min^{-1} heating mode, showed an increase in cell size at 250 K, with the *b*-axis reaching 16.9 Å and *V* reaching 5265 Å^3. The onset of cell shrinkage occurred at higher temperatures using the faster scan rate, reflected by the cell volume of 5165 Å^3 at 200 K — contrasting with 5198 Å^3 measured at 190 K using the 1 K min^{-1} cooling rate. The cell parameters continued to shrink along the 4 K min^{-1} cooling mode, reaching minimum values for *b* and *V* of 16.5 Å and 5065 Å^3 at 50 K, with the heating mode approximating the same trend in the reverse direction. The low-temperature values found using the faster scan rate of 4 K min^{-1} are larger than those found when cooling at 1 K min^{-1}, and support the finding that cooling desolvated **1** at faster scan rates causes the lattice to transition with only about 50% completion (Figure 2). Additionally, the trends in unit cell parameters *b* and *V* which were established by SCXRD experiments were reproduced by PXRD, suggesting that the spin transition in the bulk material is governed by the same or a similar mechanism to that observed in single crystals and the above magnetic susceptibility.

3. Conclusion

In summary, we present a new Fe(II) dinuclear helicate **1** which undergoes SCO that is incomplete in single crystals of **1** but complete in bulk solvated **1**. Desolvated **1** may achieve complete SCO at slow scan rates (1 K min^{-1}) and incomplete SCO at faster scan rates (4, 7 and 10 K min^{-1}). The manipulation of the SCO profile by the temperature scan rate is shown to be associated with occupation of structurally distinct phases in the solid. Both phases have their own corresponding HS and LS states, allowing the material to conform to one of four states: **HS-a**, **LS-**

a, **HS-b** and **LS-b**. This allows for kinetic control of the SCO profile exhibited by the solid, as different scan rates can alter the resultant SCO behavior. Interconversion between distinct HS or LS phases was demonstrated by the deviation that was observed between the cooling and heating modes in the magnetic susceptibility studies. VT-SCXRD studies, corroborated with VT-PXRD, showed that the full relaxation pathway to **LS-a** was facilitated by contraction along the *b*-axis, while this contraction was inhibited by fast cooling, causing a transition to **LS-b**.

Our study demonstrates the degree of multifunctionality which can be manifested in SCO materials, facilitated by the supramolecular environment. Steric influences between SCO molecules can be used to convert between distinct structural phases, and when controlled by scan rate, diverse magnetic behavior can occur. This work may forge avenues by which the control of dinuclear [HS-LS] ↔ [LS-HS] equilibria can be investigated and manipulated in the solid state, potentially aiding the design of next-generation signaling and logic materials.

4. Materials and Methods

4.1. Synthetic Procedures

1-(Pyridine-4-yl)-1H-imidazole-4-carbaldehyde was synthesized from the procedure that was previously reported.[43]

Synthesis of ligand **L**: 4,4'-oxydianiline (1140 mg, 5.7 mmol, 1 eq) was dissolved in 30 mL of EtOH and added dropwise to 1-(pyridine-4-yl)-1H-imidazole-4-carbaldehyde (2027 mg, 10.6 mmol, 2 eq) in 70 mL of EtOH. The reaction mixture was heated at reflux with stirring for 4 h, after which pale white precipitate formed. This was collected by filtration and was washed with cold EtOH to give **L** as a pale white powder. Yield: 2301 mg, 79.2%. ^{1}H NMR (DMSO-d_6, 400

MHz) δ (ppm); 8.725 (s, 1H), 8.709 (d, 2H), 8.629 (s, 1H), 8.530 (s, 1H), 7.901 (d, 2H), 7.329 (d, 2H), 7.078 (d, 2H); ^{13}C NMR (DMSO-d_6, 100 MHz) δ (ppm); 155.47, 153.85, 151.93, 147.43, 143.06, 142.15, 137.35, 122.98, 119.79, 119.63, 114.53; HR-ESI MS (positive ion detection, EtOH): *m/z* (calcd, exp) = [**L**+H]$^+$; 511.1195, 511.2010; [**L**+Na]$^+$; 533.1815, 533.1523.

Synthesis of **1**·6H_2O: Iron(II) tetrafluoroborate hexahydrate (747 mg, 2.2 mmol, 2 eq) was dissolved in 75 mL of MeCN and added dropwise to a suspension of **L** (1754 mg, 3.4 mmol, 3 eq) in 125 mL of MeCN. The reaction mixture was heated at reflux for 1 h with stirring, resulting in a clear orange solution. After filtration, slow vapor diffusion of diethyl ether into the reaction mixture over two weeks led to the formation of orange plate crystals. These were collected by gravity filtration and air dried before analysis. Yield: 554 mg, 23.6%; Elemental analysis (%) (calcd, exp) for $C_{90}H_{66}N_{24}O_3Fe_2B_4F_{16}$·6$H_2O$): C (51.48, 51.51), H (3.75, 4.08), N (16.02, 16.16); HR-ESI MS (positive ion detection, MeCN): *m/z* (calcd, exp) = [Fe_2**L**$_3$]$^{4+}$, 410.6124, 410.5572; [Fe_2**L**$_3$(BF_4)]$^{3+}$; 576.4847, 576.4459; [Fe_2**L**$_3$(BF_4)$_2$]$^{2+}$; 908.2300, 908.1909.

2.2. Physical Measurements

High resolution ESI-MS experiments were performed using a Waters Xevo QToF mass spectrometer (Waters, Milford, MA, USA), operating in positive ion mode. The ligand was dissolved in EtOH and the metal complex was dissolved in MeCN. The samples were infused directly into the ESI source via a syringe. Nuclear magnetic resonance (NMR) data was acquired at the Biomedical Magnetic Resonance Facility (Western Sydney University) using a Bruker Avance 400 MHz NMR spectrometer. CHN analysis was carried out at Kumamoto University, Japan. Simultaneous thermal analysis (STA) was conducted on a NETZSCH STA449 Jupiter

instrument using aluminium crucible. STA measurements were acquired using Argon for both the purge and protective gases; the temperature range of 303-863 K was cycled at 10 K min^{-1}.

Raman spectroscopy was performed using an inVia Qontor Raman microspectrometer (Renishaw, UK) using a 2400 lines mm^{-1} grating and a 100 mW 514 nm diode laser. The polycrystalline powder sample **1**·$6H_2O$ was deposited directly into a Linkam THMS600 variable temperature stage, and controlled cooling at 1 K min^{-1} was used to sequentially ramp from 301 K to each temperature in the series. Static scans measuring from 511 - 1804 cm^{-1} for all datasets. 1% laser power (0.89 mW) was used to acquire most spectra, and 10% power (8.9 mW) was used to cause a LIESST excitation at 100 K.

Scanning Electron Microscopy (SEM) and Energy Dispersive Spectroscopy (EDS) spot analysis were acquired using a Phenom XL in low vacuum with a chamber pressure of 60 Pa and an accelerating voltage of 15 kV. All samples were mounted on an aluminium stub with double-sided conductive carbon tape and then imaged uncoated. Spot EDS analysis was carried out using Phenom EDS software with a silicon drift detector (SDD).

To collect **1**@100/relax, a suitable single crystal of **1** was selected under a polarizing microscope (Leica M165Z) and mounted on a MicroMount (MiTeGen, USA) consisting of a thin polymer tip with a wicking aperture. The X-ray diffraction measurements were carried out on a Bruker D8 Quest Single Crystal diffractometer with Photon II detector using a IμS 3.0 Microfocus source with Mo-Kα radiation (λ = 0.710723 Å). The single crystal, mounted on the goniometer using cryo loops for intensity measurements, was coated with paraffin oil and quickly transferred to the cold stream using an Oxford Cryo stream 800 attachment. The crystal was mounted at 250 K for screening, and after 1 h was cooled at 2 K min^{-1} to 100 K for collection of the full dataset.

Symmetry related absorption correction using the program SADABS[45] were applied and the data were corrected for Lorentz and polarization effects using Bruker APEX 3 software.[46] The structure was solved by ShelXT using intrinsic phasing[47] and full matrix least-square refinements were carried out using ShelXL[48,49] and olex2 graphical user interface.[50]

All other single crystal data was collected employing the MX1 beamline at the Australian Synchrotron using silicon double crystal monochromated radiation (λ = 0.71073 Å).[51] For each structure, two collections were taken, each consisting of a sweep through θ of 360°, but differing by the setting of κ to 0 or 180°. For **1**@100/flash, a crystal of **1** was mounted at 100 K and scanned after instrument setup. For each scan rate-dependent experiment a crystal of **1** was selected and mounted at 250 K. After collecting a full dataset, the temperature was reduced at the specified scan rate to the next specified temperature, followed by data collection, down to the minimum temperature of 100 K. XDS software[52] was used for data integration, processing, scaling and the merging of raw datasets. The empirical absorption correction was then applied at the synchrotron using SADABS.[45] The structure was solved with ShelXT[47] using the intrinsic phasing method and the full-matrix least-squares refinements were carried out using a suite of SHELX programs[48,49] via the Olex2 interface.[50] Refinement details can be found in the ESI (S7). The crystallographic data in CIF format has been deposited at the Cambridge Crystallographic Data Centre with CCDC nos. 2215597 - 2215608. It is available free of charge from the Cambridge Crystallographic Data Centre, 12 Union Road, Cambridge CB2 1 EZ, UK; fax: (+44) 1223-336-033; or e-mail: deposit@ccdc.cam.ac.uk.

PXRD measurements were carried out in Empyrean X-Ray Diffractometer (Supplier: PANalytical BV) fitted with a Copper tube (λ = 1.5406 Å) and a PIXcel detector. In order to enable data collection at low temperature and at controlled temperature variation rate, the sample stage was

configured with Oxford PheniX cryostat. Raw data collection was performed over the 2θ range of 5° to 40° with step size 0.013° and 995s measurement time per step. A full pattern Pawley fit using HighScore Plus software (Supplier: PANalytical BV) was performed on the PXRD scans using the cif obtained from SCXRD to extract unit cell parameters at each temperature.

Magnetic susceptibility measurements were conducted using a Quantum Design SQUID magnetometer calibrated against a standard palladium sample. The solvated sample was collected from diffusion vials before air drying. Magnetic susceptibility measurements were collected at scan rates of 1 and 4 K min^{-1} in the cooling and heating modes. Desolvation was achieved by holding samples at an isotherm of 400 K for 30 minutes, and cooling and heating runs were collected for this desolvated sample at scan rates of 1, 4, 7 and 10 K min^{-1}. LIESST studies were conducted on solvated and desolvated samples under red (800 nm) and green (532 nm) laser irradiation. For each measurement, the sample was irradiated with the selected light source at 5 K until saturation of the magnetic signal, after which the sample was heated at 1 K min^{-1}. Measurements were taken under an applied field of 0.5 T at a scan rate of 1, 4, 7 and 10 K min^{-1}.

Mössbauer experiments were performed using a Wissel MVT-1000 Mössbauer spectrometer with a ^{57}Co/Rh source in a constant-acceleration transmission spectrometer (Topologic Systems) equipped with a closed-cycle helium refrigerator cryostat (Iwatani Co., Ltd.). All isomer shifts are given relative to α-Fe at room temperature.

ASSOCIATED CONTENT

The Supporting Information is available free of charge on the ACS Publications website at: ____

Physical measurements, Mössbauer, SQUID and LIESST analysis, Raman spectroscopy, Scaling of crystal packing coefficient and molecular volume, helicate structural parameters, intermolecular interactions of **1** and crystallographic refinement details (PDF).

CCDC nos. 2215597 – 2215608 contain the supplementary crystallographic data for this paper. These data can be obtained free of charge via www.ccdc.cam.ac.uk, or by emailing data_request@ccdc.cam.ac.uk, or by contracting the Cambridge Crystallographic Data Center, 12 Union Road, Cambridge CB2 1EZ, UK; fax: + 44 1223 336033.

AUTHOR INFORMATION

Corresponding Author

Feng Li - *School of Science, Western Sydney University, Locked Bag 1797, Penrith NSW 2751, Australia;* Email: feng.li@westernsydney.edu.au

Authors

Matthew J. Wallis - *School of Science, Western Sydney University, Locked Bag 1797, Penrith NSW 2751, Australia*

Alexander R. Craze - *School of Science, Western Sydney University, Locked Bag 1797, Penrith NSW 2751, Australia*

Hikaru Zenno - *Department of Chemistry, Graduate School of Science and Technology, Kumamoto University, 2-39-1 Kurokami, Chuo-ku, Kumamoto 860-8555, Japan*

Ryuya Tokunaga - *Department of Chemistry, Graduate School of Science and Technology, Kumamoto University, 2-39-1 Kurokami, Chuo-ku, Kumamoto 860-8555, Japan*

Takahiro Taira - *Department of Chemistry, Graduate School of Science and Technology, Kumamoto University, 2-39-1 Kurokami, Chuo-ku, Kumamoto 860-8555, Japan*

Hyunsung Min - *School of Science, Western Sydney University, Locked Bag 1797, Penrith NSW 2751, Australia*

Mohan M. Bhadbhade - *Mark Wainwright Analytical Centre, University of New South Wales, Kensington, NSW, 2052, Australia*

Saroj Kumar Bhattacharyya - *Mark Wainwright Analytical Centre, University of New South Wales, Kensington, NSW, 2052, Australia*

Ruoming Tian - *Mark Wainwright Analytical Centre, University of New South Wales, Kensington, NSW, 2052, Australia*

Anne M. Rich - *Mark Wainwright Analytical Centre, University of New South Wales, Kensington, NSW, 2052, Australia*

Shinya Hayami - *Department of Chemistry, Graduate School of Science and Technology, Kumamoto University, 2-39-1 Kurokami, Chuo-ku, Kumamoto 860-8555, Japan*

Jack K. Clegg - *School of Chemistry and Molecular Bioscience, The University of Queensland St Lucia, QLD 4072, Australia*

Christopher E. Marjo - *Mark Wainwright Analytical Centre, University of New South Wales, Kensington, NSW, 2052, Australia*

Leonard F. Lindoy - *School of Chemistry F11, The University of Sydney, NSW 2006, Australia*

Present Addresses

Alexander R. Craze - *Department of Chemistry, University of Oxford, 12 Mansfield Road, Oxford OX1 3TA, UK*

NOTES

There are no conflicts to declare.

ACKNOWLEDGMENTS

The authors would like to thank Western Sydney University (WSU) for research funding, the Biomedical Magnetic Resonance Facility (BRMF), the Advanced Materials Characterisation Facility (AMCF) at WSU, Kumamoto University and the Mark Wainwright Analytical Centre at the University of New South Wales (UNSW). CHN analysis, magnetic and Mössbauer measurements were performed at Kumamoto University. Crystallographic data was collected at both the Mark Wainwright Analytical Centre at UNSW Sydney, and the MX1 beamline of the Australian Synchrotron, Clayton, Victoria, Australia. We also thank the Australian Synchrotron for travel support and their staff for beamline assistance.

REFERENCES

1. Molnár, G.; Salmon, L.; Nicolazzi, W.; Terki, F.; Bousseksou, A. Emerging properties and applications of spin crossover nanomaterials. *J. Mater. Chem. C.* **2014**, *2*, 1360-1366.
2. Tsukiashi, A.; Min, K. S.; Kitayama, H.; Terasawa, H.; Yoshinaga, S.; Takeda, M.; Lindoy, L. F.; Hayami, S. Application of spin-crossover water soluble nanoparticles for use as MRI contrast agents. *Sci. Rep*. **2018**, *8*, 1-5.
3. Kumar, K. S.; Ruben, M. Sublimable Spin-Crossover Complexes: From Spin-State Switching to Molecular Devices. *Angew. Chem. Int. Ed.* **2021**, *60*, 7502-7521.

4. McConnell, A. J. Spin-state switching in Fe(II) helicates and cages. *Supramolecular Chemistry*. **2018**, *30*, 858-868.
5. Gütlich, P.; Gaspar, A. B.; Garcia, Y. Spin state switching in iron coordination compounds. *Beilstein J. Org. Chem.* **2013**, *9*, 342-391.
6. Brooker, S. Spin crossover with thermal hysteresis: practicalities and lessons learnt. *Chem. Soc. Rev.* **2015**, *44*, 2880-2892.
7. Hogue, R. W.; Singh, S.; Brooker, S. Spin crossover in discrete polynuclear iron(II) complexes. *Chem. Soc. Rev.* **2018**, *47*, 7303-7338.
8. Bousseksou, A.; Molnár, G.; Real, J. A.; Tanaka, K. Spin crossover and photomagnetism in dinuclear iron(II) compounds. *Coord. Chem. Rev.* **2007**, *251*, 1822-1833.
9. Li, L.; Neville, S. M.; Craze, A. R.; Clegg, J. K.; Sciortino, N. F.; Athukorala Arachchige, K. S.; Mustonen, O.; Marjo, C. E.; McRae, C. R.; Kepert, C. J.; Lindoy, L. F.; Aldrich-Wright, J. R.; Li, F. Spin-State Patterning in an Iron(II) Tripodal Spin-Crossover Complex. *ACS Omega*. **2017**, *2*, 3349-3353.
10. Li, L.; Craze, A. R.; Mustonen, O.; Zenno, H.; Whittaker, J. J.; Hayami, S.; Lindoy, L. F.; Marjo, C. E.; Clegg, J. K.; Aldrich-Wright, J. R.; Li, F. A mixed-spin spin-crossover thizolylimine $[Fe_4L_6]^{8+}$ cage. *Dalton Trans.* **2019**, *48*, 9935-9938.
11. Li, L.; Saigo, N.; Zhang, Y.; Fanna, D. J.; Shepherd, N. D.; Clegg, J. K.; Zheng, R.; Hayami, S.; Lindoy, L. F.; Aldrich-Wright, J. R.; Li, C-G.; Reynolds, J. K.; Harman, D. G.; Li, F. A large spin-crossover $[Fe_4L_4]^{8+}$ tetrahedral cage. *J. mater. Chem. C.* **2015**, *3*, 7878-7882.
12. Scott, H. S.; Staniland, R. W.; Kruger, P. E. Spin crossover in homoleptic Fe(II) imidazolylimine complexes. *Coord. Chem. Rev.* **2018**, *362*, 24-43.

13. Halcrow, M. A. The Effect of Ligand Design on Metal Ion Spin State - Lessons from Spin Crossover Complexes. *Crystals*. **2016**, *6*, 58-78.

14. Ni, Z-P.; Liu, J-L.; Hoque, N. M.; Liu, W.; Li, J-Y.; Chen, Y-C.; Tong, M-L. Recent advances in guest effects on spin-crossover behavior in Hofmann-type metal-organic frameworks. *Coord. Chem. Rev.* **2016**, *335*, 28-43.

15. Telfer, S. G.; Bocquet, B.; Williams, A. F. Thermal Spin Crossover in Binuclear Iron(II) Helicates: Negative Cooperativity and a Mixed Spin State in Solution. *Inorg. Chem.* **2001**, *40*, 4818-4820.

16. Ortega-Villar, N.; Muñoz, M. C.; Real, J. A. Symmetry Breaking in Iron(II) Spin-Crossover Molecular Crystals. *Magnetochemistry*. **2016**, *2*, 16-38.

17. Klingele, M. H.; Moubaraki, B.; Cashion, J. D.; Murray, K. S.; Brooker, S. The first X-ray crystal structure determination of a dinuclear complex trapped in the [low spin-high spin] state: $[Fe^{II}_2(PMAT)_2](BF_4)_4$.DMF. *Chem. Comm.* **2004**, 987-989.

18. Hogue, R. W.; Feltham, H. L. C.; Miller, R. G.; Brooker, S. Spin Crossover in Dinuclear N_4S_2 Iron(II) Thioether-Triazole Complexes: Access to [HS-HS], [HS-LS], and [LS-LS] States. *Inrog. Chem.* **2016**, *55*, 4152-4165.

19. Aleshin, D. Y.; Diego, R.; Barrios, L. A.; Nelyubina, Y. V.; Aromí, G.; Novikov, V. V. Unravelling of a [High Spin - Low Spin] ↔ [Low Spin - High Spin] Equilibrium in Spin-Crossover Iron(II) Dinuclear Helicates Using Paramagnetic NMR Spectroscopy. *Angew. Chem. Int. Ed.* **2022**, *61*, 1-6.

20. Barrios, L. A.; Diego, R.; Darawsheh, M.; Martinez, J. I.; Roubeau, O.; Aromi, G. A ferric guest inside a spin crossover ferrous helicate. *Chem. Comm.* **2022**, *58*, 5375-5378.

21. Craze, A. R.; Bhadbhade, M. M.; Komatsumaru, Y.; Marjo, C. E.; Hayami, S.; Li, F. A Rare Example of a Complete, Incomplete, and Non-Occurring Spin Transition in a $[Fe_2L_3]X_4$ Series Driven by a Combination of Solvent-and Halid-Anion-Mediated Steric Factors. *Inorg. Chem.* **2020**, *59*, 1274-1283.

22. Howard-Smith, K. J.; Craze, A. R.; Zenno, H.; Yagyu, J.; Hayami, S.; Li, F. A large dinuclear Fe(II) triple helicate demonstrating a two-step spin crossover. *Chem. Comm.* **2020**, *56*, 8838-8841.

23. Palleteret, D.; Clérac, R.; Mathoniére, C.; Harté, E.; Schmitt, W.; Kruger, P. E. Asymmetric spin crossover behaviour and evidence of light-induced excited spin state trapping in a dinuclear iron(II) helicate. *Chem. Comm.* **2009**, 221-223.

24. Singh, S.; Brooker, S. Correlations between ligand field Δ_o, spin crossover $T_{1/2}$ and redox potential E_{pa} in a family of five dinuclear helicates. *Chem. Sci.* **2021**, *12,* 10919-10929.

25. Li, L.; Craze, A. R.; Akiyoshi, R.; Tsukiashi, A.; Hayami, S.; Mustonen, O.; Bhadbhade, M. M.; Bhattacharyya, S.; Marjo, C. E.; Wang, Y.; Lindoy, L. F.; Aldrich-Wright, J. R.; Li, F. Direct monitoring of spin transitions in a dinuclear triple-stranded helicate iron(II) complex through X-ray photoelectron spectroscopy. *Dalton Trans.* **2018**, *47*, 2543-2548.

26. Craze, A. R.; Sciortino, N. F.; Bhadbhade, M. M.; Kepert, C. J.; Marjo, C. E.; Li, F. Investigation of the Spin Crossover Properties of Three Dinuclear Fe(II) Triple Helicates by Variations of the Steric Nature of the Ligand Type. *Inorganics*, **2017**, *5*, 62-75.

27. Sunatsuki, Y.; Kawamoto, R.; Fujita, K.; Maruyama, H.; Suzuki, T.; Ishida, H.; Kojima, M.; Lijima, S.; Matsumoto N. Structures and Spin States of Bis(tridentate)-Type

Mononuclear and Triple Helicate Dinuclear Iron(II) Complexes of Imidazole-4-carbaldehyde azine. *Inorg. Chem.* **2009**, *48*, 8784-8795.

28. Archer, R. J.; Hawes, C. S.; Jameson, G. N. L.; McKee, V.; Moubaraki, B.; Chilton, N. F.; Murray, K. S.; Schmitt, W.; Kruger, P. E. Partial spin crossover behavior in a dinuclear iron(II) triple helicate. *Dalton Trans.* **2011**, *40*, 12368-12373.

29. Craze, A. R.; Zenno, H.; Pfrunder, M. C.; McMurtrie, J. C.; Hayami, S.; Clegg, J. K.; Li, F. Supramolecular Modulation of Spin Crossover in an Fe(II) Dinuclear Triple Helicate. *Inorg. Chem.* **2021**, *60*, 6731-6738.

30. Lu, Y.; Lent, C. S. A metric for characterizing the bistability of molecular quantum-dot cellular automata. *Nanotechnology*, **2008**, *19*, 155703.

31. Schneider, B.; Demeshko, S.; Neudeck, S.; Dechert, S.; Meyer, F. Mixed-spin [2 x 2] Fe_4 grid complex optimized for quantum cellular automata. *Inorg. Chem.* **2013**, *52*(22), 13230-13237.

32. Weihermüller, J.; Stephan Schlamp, S.; Birger Dittrich, B.; Weber, B. Kinetic Trapping Effects in Amphiphilic Iron(II) Spin Crossover Compounds. *Inorganic Chem*. **2019** *58,* (2), 1278-1289.

33. Craig, G. A.; Costa, J. S.; Teat, S. J.; Roubeau, O.; Yufit, D. S.; Howard, J. A. K.; Aromí, G. Multimetastability in a Spin-Crossover Compound Leading to Different High-Spin-to-Low-Spin Relaxation Dynamics. *Inorg. Chem.* **2013** *52* (12), 7203-7209.

34. Schönfeld, S.; Lochenie, C.; Thoma, P.; Weber, B. 1D iron(II) spin crossover coordination polymers with 3,3′-azopyridine – kinetic trapping effects and spin transition above room temperature. *CrystEngComm*. **2015**, *17*, 5389-5395

35. Seredyuk, M.; Muñoz, M.C.; Castro, M.; Romero-Morcillo, T.; Gaspar, A.B.; and Real, J.A. Unprecedented Multi-Stable Spin Crossover Molecular Material with Two Thermal Memory *Channels. Chem. Eur. J.* **2013**, *19*, 6591-6596.

36. Deng, Y-F.; Wang, Y-N.; Zhao, X-H.; Zhang, Y-Z. Desolvation–Solvation-Induced Reversible On–Off Switching of Two Memory Channels in a Cobalt(II) Coordination Polymer: Overlay of Spin Crossover and Structural Phase Transition. *CCS Chem.* **2022**, *4*, 3064-3075.

37. Yamasaki, M.; Ishida, T. Heating-rate dependence of spin-crossover hysteresis observed in an iron(II) complex having tris(2-pyridyl)methanol. *J. Mater. Chem. C.* **2015**, *3*, 7784-7787

38. Reichel, F.; Clegg, J. K.; Gloe, K.; Gloe, K; Weigand, J. J.; Reynolds, J. K.; Li, C-G; Aldrich-Wright, J. R.; Kepert, C. J.; Lindoy, L. F.; Yao, H-C; Li, F. Self-assembly of an imidazolate-bridged FeIII/CuII heterobimetallic cage. *Inorg. Chem.* **2014**, *53*(2), 688-690

39. Li, L.; Fanna, D. J.; Shepherd, N. D.; Lindoy, L. F.; Li, F. Constructing coordination nanocages: the metalloligand approach. *J. Incl. Phenom. Macrocycl. Chem.* **2015**, *82*, 3–12.

40. Li, L.; Zhang, Y.; Avdeev, M.; Lindoy, L. F.; Harman, D. G.; Zheng, R.; Cheng, Z.; Aldrich-Wright, J. R.; Li, F. Self-assembly of a unique 3d/4f heterometallic square prismatic box-like coordination cage. *Dalton Trans*. **2016**, *45*, 9407-9411

41. Li, L.; Craze, A. R.; Fanna, D. J.; Brock, A. J.; Clegg, J. K.; Lindoy, L. F.; Aldrich-Wright, J. R.; Reynolds, J. K.; Li, F. Synthesis and characterisation of two Cu(I) metalloligands based on tetradentate tripodal ligands. *Polyhedron*. **2017**, *125*, 44-49.

42. Li, F.; Lindoy, L. F. Metalloligand Strategies for Assembling Heteronuclear Nanocages – Recent Developments. *Aust. J. Chem.* **2019**, *72*, 731-741.

43. Min, H.; Craze, A. R.; Taira, T.; Wallis, M. J.; Bhadbhade, M. M.; Tian, R.; Fanna, D. J.; Wuhrer, R.; Hayami, S.; Clegg, J. K.; Marjo, C. E.; Lindoy, L. F.; Li, F. Self-Assembly of a Rare High Spin Fe^{II}/Pd^{II} Tetradecanuclear Cubic Cage Constructed via the Metalloligand Approach. *Chemistry.* **2022**, *4*, 535-547.

44. Halcrow, M. A. Structure:function relationships in molecular spin-crossover complexes. *Chem. Soc. Rev*. **2011**, *40*, 4119–4142

45. SADABS, version 2014/5; Bruker AXS Inc., Madison, WI, USA, **2001**.

46. APEX3, SAINT and SADABS. Bruker AXS INC., Madison, WI, USA, **2016**.

47. Sheldrick, G. M. SHELXT—Integrated space-group and crystal-structure determination. Acta. Cryst. A **2015**, 71, 3–8.

48. Sheldrick, G. M. SHELX-2014: Programs for Crystal Structure Analysis; University of Göttingen: Göttingen, Lower Saxony, Germany, **2014**.

49. Sheldrick, G. M. Crystal structure refinement with SHELXL. *Acta. Cryst. C.* **2015**, 71, 3–8.

50. Dolomanov, O. V.; Bourhis, L. J.; Gildea, R. J.; Howard, J. A. K.; Puschmann, H. OLEX2: A complete structure solution, refinement and analysis program. *J. Appl. Cryst.* **2009**, 42, 339–341.

51. Cowieson, N. P.; Aragao, D.; Clift, M.; Ericsson, D. J.; Gee, C.; Harrop, S. J.; Mudie, N.; Panjikar, S.; Price, J. R.; Riboldi-Tunnicliffe, A.; et al. MX1: A bending-magnet crystallography beamline serving both chemical and macromolecular crystallography communities at the Australian Synchrotron. *J. Synchrotron Rad.* **2015**, 22, 187–190.

52. Kabsch, W. XDS. Automatic processing of rotation diffraction data from crystals of initially unknown symmetry and cell constants. *J. Appl. Crystallogr.* **1993**, 26, 795–800.